Seventh International Conference on Computational Fluid Dynamics (ICCFD7), Big Island, Hawaii, July 9-13, 2012

ICCFD7-2012-xxxx

A Summary of Data and Findings from the First Aeroelastic Prediction Workshop

David M. Schuster, Pawel Chwalowski, Jennifer Heeg, Carol D. Wieseman
Corresponding author: david.m.schuster@nasa.gov

NASA Langley Research Center, USA

Abstract: This paper summarizes data and findings from the first Aeroelastic Prediction Workshop (AePW) held in April, 2012. The workshop has been designed as a series of technical interchange meetings to assess the state of the art of computational methods for predicting unsteady flowfields and static and dynamic aeroelastic response. The goals are to provide an impartial forum to evaluate the effectiveness of existing computer codes and modeling techniques to simulate aeroelastic problems, and to identify computational and experimental areas needing additional research and development. For this initial workshop, three subject configurations have been chosen from existing wind tunnel data sets where there is pertinent experimental data available for comparison. Participant researchers analyzed one or more of the subject configurations and results from all of these computations were compared at the workshop.

Keywords: Unsteady Aerodynamics, Aeroelasticity, Computational Fluid Dynamics, Transonic Flow, Separated Flow.

1 Introduction

The Aeroelastic Prediction Workshop (AePW) has been patterned after two very successful workshops conducted over the past decade: the Drag Prediction Workshop[1] and the High Lift Prediction Workshop[2]. The AePW assembles an international slate of participants to analyze a carefully selected set of unsteady aerodynamics and aeroelastic problems for which experimental validation data is available. The intent of the workshop is to investigate the ability of our present computational aeroelastic tools to predict nonlinear aeroelastic phenomena, particularly those arising from the formation of shock waves, vortices, and separated flow.

Many static and dynamic aeroelastic phenomena are influenced by, or a direct result of, these nonlinear flow phenomena. Static aeroelastic loadings and deflections, reduced control effectiveness, control reversal, and structural divergence boundaries can be a strong function of these nonlinear aerodynamic phenomena, particularly when aerospace vehicles are operating away from their nominal design point. Dynamic aeroelastic problems such as buffet, control surface buzz and other limit cycle oscillations are a direct result of some type of nonlinearity, whether it is structural or aerodynamic. Flow nonlinearities, particularly separated flow, can limit the amount of aerodynamic load that can be applied to a structure and cause otherwise divergent aeroelastic instabilities, like flutter, to become a limited-amplitude oscillation prior to structural failure. In the case of classical flutter, this limiting of the dynamic divergence could be considered beneficial since it could avoid a catastrophic structural failure. However, the structural oscillations could still be quite large resulting in other system failures and/or loss of vehicle control. Buffeting and control surface buzz are two other examples of nonlinear aeroelastic phenomena that can be problematic for aerospace vehicles. These phenomena can often be relatively high frequency in nature, and even though the magnitude of the structural oscillations might be small, the number of structural oscillations could be large, even for a short duration event.

Thus structural fatigue and degradation of structural service life become a concern when these phenomena are encountered.

The present state-of-the-art for production aeroelastic analysis is the coupling of linear aerodynamic theory with linear structural dynamics models. There are a number of commercial products on the market today that are capable of performing this type of analysis. They can compute both static and dynamic aeroelastic simulations, including flutter and are well understood for subsonic and supersonic flows over low-disturbance aerospace vehicles. However, at transonic conditions and for geometries where nonlinear aerodynamics or nonlinear structures are important, these methods quickly lose accuracy and become less dependable. This is particularly true in the transonic flight regime where shock waves form on the vehicle surface that can transiently separate the flow boundary layer. High flow incidence angles, and complex vehicle geometries and protuberances can produce similar effects. Large structural deformations, as in those that might occur on very high aspect ratio wings can also result in aeroelastic nonlinearity. For these situations, nonlinear aerodynamic and/or nonlinear structural analysis are required, significantly complicating the aeroelastic analysis.

Aeroelastic analysis requires the coupling of a structural representation with an aerodynamic model and the two disciplines must be simulated in a coupled manner. Sometimes assumptions or errors in the aerodynamic simulation can be masked by assumptions and errors in the structural model, and vice versa. In an attempt to limit or at least minimize this issue, it is typically desirable to first analyze and evaluate these two disciplines in an uncoupled manner prior to coupling them for an aeroelastic simulation. Thus the AePW Organizing Committee (OC), see Table 1, has decided to initially focus on test cases that stress the unsteady aerodynamic prediction component of the problem and minimize the aeroelastic coupling required to simulate the cases. Future workshops hope to introduce stronger aeroelastic coupling as an improved understanding of the uncoupled aerodynamic and structural analysis capability is formed. The AePW OC established the further objective of selecting test cases that provided a relatively simple nonlinear flow situation where it was suspected that the computational aeroelasticity methods would have a high probability of accurately simulating the unsteady aerodynamics problem as well as increasingly complex problems that would stress the computational aerodynamics state-of-of-the-art. As a result, the AePW OC selected three datasets for the initial workshop, all of which have detailed unsteady aerodynamic wind tunnel data under forced oscillation test conditions.

Table 1. Aeroelastic Prediction Workshop Organizing Committee.

Name	Affiliation
Bhatia, Kumar	Boeing Commercial Aircraft, USA
Ballmann, Josef	Aachen University, Germany
Blades, Eric	ATA Engineering, Inc., USA
Boucke, Alexander	Aachen University, Germany
Chwalowski, Pawel	NASA, USA
Dietz, Guido	European Transonic Windtunnel (ETW), Germany
Dowell, Earl	Duke University, USA
Florance, Jennifer	NASA, USA
Hansen, Thorsten	ANSYS Germany GmbH, Germany
Heeg, Jennifer	NASA, USA
Mani, Mori	Boeing Research & Technology, USA
Mavriplis, Dimitri	University of Wyoming, USA
Perry, Boyd	NASA, USA
Ritter, Markus	DLR, Germany
Schuster, David	NASA, USA
Smith, Marilyn	Georgia Institute of Technology, USA
Taylor, Paul	Gulfstream Aerospace, USA
Whiting, Brent	Boeing Research & Technology, USA
Wieseman, Carol	NASA, USA

Two of the cases, the Rectangular Supercritical Wing (RSW) [3]-[6] and the Benchmark Supercritical Wing (BSCW) [7]-[9] are simple, structurally rigid, rectangular planform wings that are oscillated at a specified pitch amplitude and frequency. The cases selected for analysis represent off-design conditions and involve strong shocks and separated flow, which are key ingredients to accurately predicting many nonlinear aeroelastic phenomena. The BSCW case includes a "blind" test case where experimental data were not be provided to the participants prior to the workshop. This case exhibited some unique flow behavior that challenges to today's methods. The third case selected for this initial workshop was the High Reynolds Number Aero-Structural Dynamics (HIRENASD)[10]-[16] wing tested in the European Transonic Wind Tunnel. This wing is geometrically more complex than the previous rectangular planform wings, and the wind tunnel model has a small amount of measured structural flexibility that is used to oscillate the wing in its structural modes and acquire unsteady aerodynamic data for these oscillations. This case represents a step toward a coupled aeroelastic analysis since the wing is oscillated in one of its structural modes to generate the unsteady flow.

In June, 2011, the AePW was formally initiated at the International Forum on Aeroelasticity and Structural Dynamics held in Paris, France[17]. At this meeting, the objectives of the workshop and pertinent information required to participate in the event were provided to prospective analysts. A website was established (https://c3.nasa.gov/dashlink/projects/47/) where analysts and other interested parties could obtain participation information, modeling and analysis guidelines, test case configuration data, experimental comparison data, computational grids, and other reference materials. This public site is still in operation today, and now contains a record of the analyses completed for the first AePW and future AePW plans. Computational grids for the various configurations were developed by the AePW OC and distributed to the registered workshop participants. Participants analyzed the three workshop configurations for approximately nine months, submitting their results in March, 2012. The AePW itself was held on April 21-22 in Honolulu, Hawaii, just prior to the AIAA 28th Structures, Structural Dynamics, and Materials Conference. The workshop consisted of 59 registered attendees. A total of 17 analysis teams from 10 nations (see Figure 1) provided a total of 26 analysis datasets for the three test cases, 6 RSW, 6 BSCW, and 14 HIRENASD.

Figure 1: Analyst teams from 10 nations participated in the first Aeroelastic Prediction Workshop.

2 Test Cases

2.1 Rectangular Supercritical Wing

The Rectangular Supercritical Wing (RSW) was the first configuration chosen as a test case for the AePW. The RSW was tested in the NASA Langley Transonic Dynamics Tunnel (TDT) in 1983 and a photograph from that test is shown in Figure 2. Figure 3 shows the geometric characteristics of the RSW. The wing is a simple rectangular planform with a wing tip of rotation. The wing has a span of 48 inches and a chord of 24 inches with a 12% thick supercritical airfoil section that is constant from wing root to tip. The wing is mounted to a relatively small splitter plate that is offset from the wind tunnel wall by approximately 6 inches. For the forced pitch oscillation cases, the wing was pitched about the 46 percent chord location. The wing was assumed to be rigid for all analyses.

This wing was originally chosen for its geometric simplicity and its transonic, but not overly challenging, aerodynamic characteristics. However, an unforeseen interaction of the wind tunnel wall with the experimental data measured on the wing made this case significantly more difficult than anticipated. A calibration of the TDT [18], conducted after this test was performed shows the wind tunnel boundary layer for the wall on which the model and splitter plate were mounted to be

Figure 2: Rectangular Supercritical Wing mounted in the NASA Langley Transonic Dynamics Tunnel.

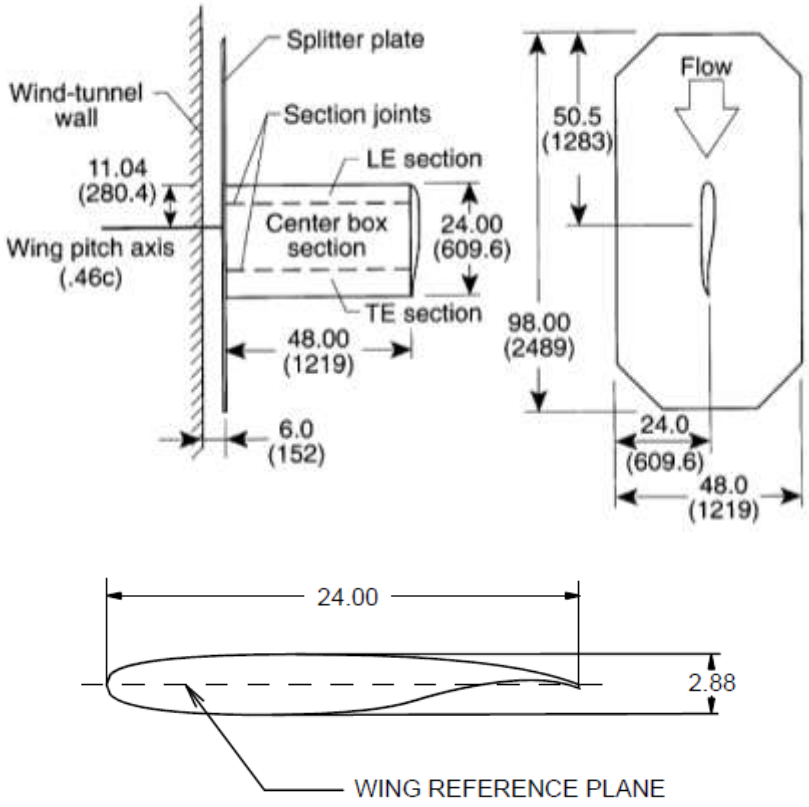

Figure 3: RSW geometric characteristics.

approximately 12 inches thick at RSW test conditions of interest. This places the RSW splitter plate well within the wind tunnel wall boundary layer. The impact of this situation on the wing pressure distribution near the wing root was not appreciated by the AePW OC prior to the wing's selection as a test case. Preliminary AePW analyses of the RSW showed the inboard pressure distributions to be

highly affected by the presence of the wind tunnel wall boundary layer. This became problematic for the AePW analysts as will be discussed in the results section of this paper, and thus made this test case considerably more difficult than the AePW OC intended.

The wing was tested in R-12 heavy gas in the TDT, and all AePW analysts performed their simulations by changing the ratio of specific heats from $\gamma = 1.4$ to $\gamma = 1.132$ to account for the differences in thermodynamic properties between air and R-12. Pressure data were measured at four constant-span stations on the wing, y/b = 0.308, 0.588, 0.809, and 0.951. These pressures include steady pressure coefficients for the static data points and pressure coefficients processed at the frequency of the forced pitch oscillation, in terms of magnitude and phase, for the dynamic data points. Reference [6] further post-processed the original magnitude and phase data into real (in-phase) and imaginary (90 degrees out-of-phase) pressure coefficient components scaled by the wing oscillation amplitude. Both data forms were supplied to the AePW analysts, but the workshop primarily focused on the magnitude and phase form of the data. There were no integrated force or moment measurements conducted in the test.

The AePW OC chose a total of four test cases for analysis by the AePW participants, two steady and two unsteady. Table 2 shows the analysis conditions chosen for the RSW.

Table 2. Rectangular Supercritical Wing analysis conditions.

Mach Number	Mean Angle of Attack (α, deg.)	Pitch Oscillation Frequency (f, Hz)	Pitch Oscillation Amplitude (θ, deg.)	Reduced Frequency $\omega C/(2V\infty)$	Reynolds Number (10^6/ft.)
0.825	2.0	0	0.0	0.0	2.0
0.825	4.0	0	0.0	0.0	2.0
0.825	2.0	10	1.0	0.152	2.0
0.825	2.0	20	1.0	0.304	2.0

2.2 Benchmark Supercritical Wing

The Benchmark SuperCritical Wing (BSCW), shown in Figure 4, was chosen as a configuration of similar geometric simplicity to the RSW case, but with flow conditions that would prove more challenging to the AePW analysts. This configuration was chosen because the experiment exhibited highly nonlinear unsteady behavior, specifically shock-separated transient flow. While there are fewer pressure measurements than for the RSW configuration, the time history data records are available for all test conditions. In addition, the BSCW experimental data chosen for this case has not been widely published. It was obtained during check-out testing of the TDT Oscillating Turntable (OTT) hardware and thus was not the focus of a computational research project. While the data is publicly available in graphical form [9], it was viewed as obscure enough to serve as the basis for a semi-blind test case. Thus the experimental data was not provided to the AePW participants prior to the actual workshop.

The BSCW has a rectangular planform as shown in Figure 5, with a NASA SC(2)-0414 airfoil. Like the RSW, the BSCW was tested in the TDT. However, the BSCW test was conducted after the TDT's conversion to R-134a as its heavy gas, so the cases for the BSCW were all computed with $\gamma = 1.116$ to account for this new test medium. The model was mounted to a large splitter plate that was offset from the TDT wall so as to place the wing closer to the center of the tunnel test section. This offset was well outside the wind tunnel wall boundary layer, so the BSCW avoided the issues with the wall boundary layer encountered on the RSW. The testing was also conducted with the sidewall slots closed, a technique which has been shown to improve the prediction of force and moment coefficients when semispan models are mounted directly to the TDT wall. The model's instrumentation is limited to one row of 40 in-situ unsteady pressure transducers at the 60% span station.

Dynamic data was obtained for the BSCW by oscillating the model in a pitching motion about the 30% chord. Steady information pertinent to this configuration is calculated as the mean value from the oscillatory time histories. The data processing performed shows small variations in the mean data due

to the forcing frequency. These variations were treated as uncertainties in the steady experimental information. The analysis conditions chosen for the BSCW are shown in Table 3.

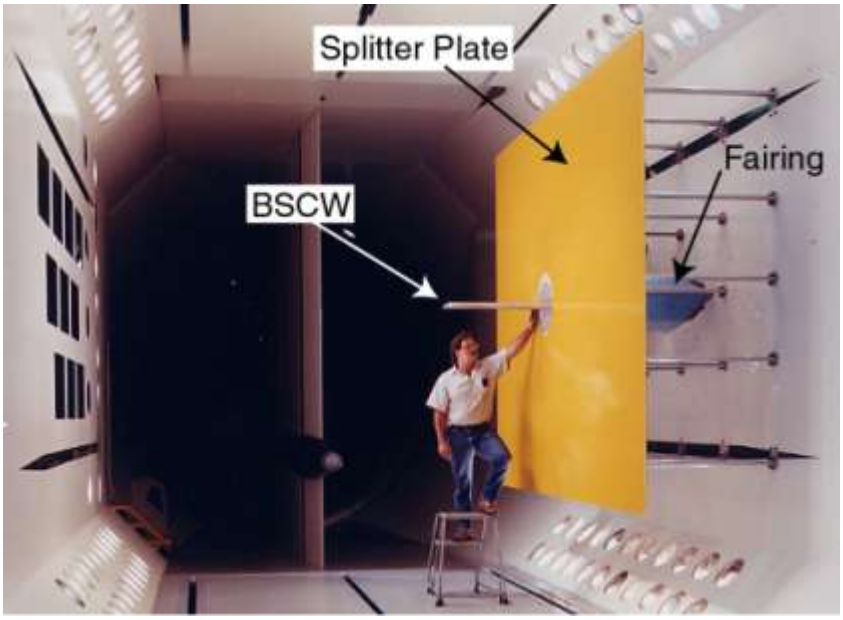

Figure 4: Benchmark Supercritical Wing mounted in the NASA Langley Transonic Dynamics Tunnel.

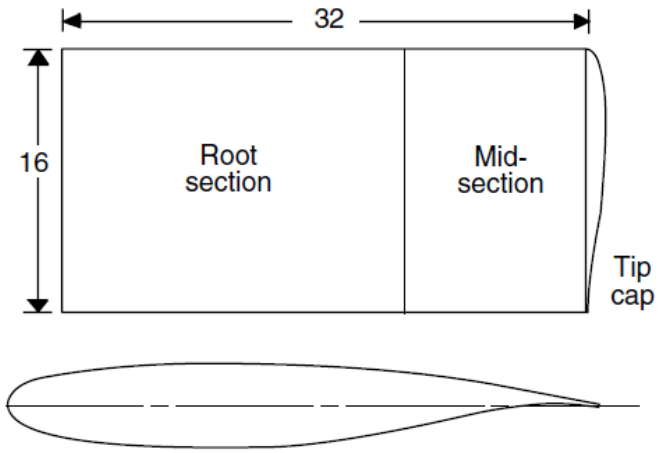

Figure 5: Planform and airfoil section for the Benchmark Supercritical Wing.

Table 3. Benchmark Supercritical Wing analysis conditions.

Mach Number	Mean Angle of Attack (α, deg.)	Pitch Oscillation Frequency (f, Hz)	Pitch Oscillation Amplitude (θ, deg.)	Reduced Frequency $\omega C/(2V\infty)$	Reynolds Number (10^6/ft.)
0.85	5.0	0	0.0	0.0	3.4
0.85	5.0	1	1.0	0.007	3.4
0.85	5.0	10	1.0	0.067	3.4

2.3 High Reynolds Number Aero-Structural Dynamics Wing

The High Reynolds Number Aero-Structural Dynamics (HIRENASD) model was the final configuration chosen for analysis in the AePW. This model was chosen as an initial coupled aeroelastic analysis configuration. The wing has a high degree of structural stiffness and broad spacing of the structural modes, which produces weak aeroelastic coupling and makes it a good entry-level basis of evaluation. The additional benefits of this data set are availability of time histories and expertise from the experimenters who are part of the AePW OC. Portions of the HIRENASD data set have been previously publicized, distributed, and analyzed [13]-[16].

HIRENASD was tested in the European Transonic Wind tunnel (ETW) in 2007. The model, as installed in this facility, is shown in Figure 6, and described by references [10]-[12]. The model has a 34 degree aft-swept, tapered clean wing, with a BAC 3-11 supercritical airfoil profile. The test article is a semi-span model, ceiling-mounted through a non-contacting fuselage fairing to a turntable, balance and excitation system, shown in Figure 7. The model and balance were designed to be very stiff, with well-separated modes. The first two wing bending modes have frequencies of approximately 27 and 79 Hz; the first wing torsion mode has a frequency of approximately 265 Hz. The model's instrumentation includes 259 in-situ unsteady pressure transducers at 7 span stations. In addition to the unsteady pressures, balance measurements and accelerations were obtained. For a small set of data points, wing displacements were also extracted via stereo pattern tracking.

Figure 6: HIRENASD wing mounted in the European Transonic Wind Tunnel.

Two types of testing were conducted: angle-of-attack polars and forced oscillations. The angle-of-attack polar data was obtained by slowly varying the angle of attack at an angular sweep rate of 0.2 degrees/second, holding all other operational parameters constant. These data were utilized primarily to provide static pressure distributions at a given test condition. The forced oscillation data was obtained by differential forcing at a specified modal frequency. All forced oscillation data to be used in the current workshop was excited near the wing's second bending modal frequency. Two Reynolds numbers, 7.0 million and 23.5 million based on reference chord, were analyzed by the AePW participants. For all cases, the Mach number is fixed at 0.80. The lower Reynolds number case has an angle of attack of 1.5 degrees, while a more challenging angle of attack of -1.34 degrees, corresponding to the zero-lift condition, was selected for analysis at the higher Reynolds number. All tests were conducted with nitrogen ($\gamma = 1.4$) as the test medium. Analysis conditions chosen for the HIRENASD wing are shown in Table 4.

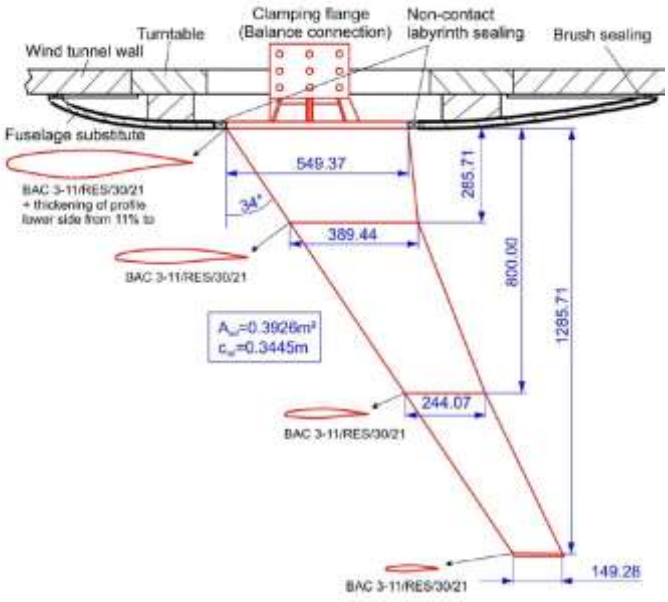

Figure 7: HIRENASD wing planform, dimensions in mm unless otherwise noted.

Table 4. HIRENASD wing analysis conditions.

Mach Number	Mean Angle of Attack (α, deg.)	Forcing Frequency (f, Hz)	2nd Bending Amplitude (Δz_t, mm)	Chord Reynolds Number ($*10^6$)
0.70	1.5	0	0.0	7.0
0.80	1.5	0	0.0	7.0
0.80	-1.34	0	0.0	23.5
0.70	1.5	79.3	2.0	7.0
0.80	1.5	78.9	2.4	7.0
0.80	-1.34	80.4	0.9	23.5

3 Aeroelastic Prediction Workshop Summary and Analysis Data

The Aeroelastic Prediction Workshop was held in Honolulu, Hawaii on April 21 – 22, 2012. Seventeen analyst teams provided computational data on the three wings selected for this initial workshop. A listing of these analysts, their affiliation and the test cases each computed is presented in Table 5. Four analysts attempted all three wings, and the vast majority of analysts computed the HIRENASD wing, most likely due to its more relevant transport aircraft geometry.

It is difficult to draw general conclusions that are applicable to all three cases. Each case had its own unique set of challenges. Certainly the most surprising result was the difficulty of the RSW case. The AePW OC had selected this case to be the simplest, and presumably most trivial case of the three, but issues with modeling the TDT wind tunnel wall boundary layer generated a surprisingly wide set of results, even for the simple steady cases. The BSCW case was chosen for its geometric simplicity but rather complex flow conditions, and like the RSW, produced a relatively wide spread of computational results. The HIRENASD configuration produced the most consistent set of computational results, despite its more complex geometry. A subset of the data and general experience with each of the test cases is presented individually.

Table 5. AEPW analysts, affiliation, and cases analyzed.

Analyst	Affiliation	RSW	BSCW	HIRENASD
Pawel Chwalowski	NASA Langley Research Center, USA	x	x	x
Thorsten Hansen	ANSYS Germany GMBH, Germany	x	x	x
Dimitri Mavriplis	University of Wyoming, USA	x	x	x
David Schuster	NASA Engineering & Safety Center, USA	x	x	
Daniel Steiling	RUAG Schweiz AG, Switzerland	x	x	x
Sebastian Timme	University of Liverpool, United Kingdom	x		
Marilyn Smith	Georgia Institute of Technology, USA		x	
Bart Eussen	NLR, The Netherlands			x
Markus Ritter	DLR , Germany			x
Mats Dahlenbring	FOI, Sweden			x
Jean Pierre Grisval	ONERA, France			x
Daniella Raveh	Technion University, Israel			x
Melike Nikbay & Z. Zhang	Istanbul TU, Turkey Zona Technologies, USA			x
Sergio Ricci	Politecnico di Milano, Italy			x
Beerinder Singh & Jack Castro	CFD++, USA MSC Nastran, USA			x
Alan Mueller & Sergey Zhelzov	CD Adapco, USA			x
Larry Brace	Boeing, USA			x

3.1 RSW Data Summary

As part of the geometry modeling and grid generation effort, members of the AePW OC conducted preliminary computations on the RSW wing to evaluate grid quality and convergence. These preliminary computations immediately uncovered an issue with how the wing was being modeled. Initial attempts simply modeled the wing from the splitter plate outboard, assuming the splitter plate to effectively behave like a plane of symmetry for a three-dimensional wing. A cursory examination of the pressure distribution for the inboard-most wing station showed the shock to be predicted much farther aft than the experimental data. Upon seeing this result, the AePW OC conducted a parametric study that investigated the modeling of the wind tunnel wall/splitter plate combination. Four geometries were investigated: wing with and without the splitter plate on an inviscid wind tunnel wall, and wing with and without the splitter plate on a viscous wind tunnel wall. For the cases without the splitter plate, the RSW wing geometry was simply extruded inboard to the actual wind tunnel wall, adding 7 inches to the total span of the wing. Not surprisingly, of the four cases, the wing on the splitter plate with the viscous wind tunnel wall produced the best results when compared with experimental data at each of the available wing stations. However, the wing without the splitter plate and the viscous wall produced results that were nearly identical to those with the splitter plate. Modeling the problem without the splitter plate simplifies the problem considerably, so the wing directly mounted to the TDT wall with a viscous wall model was chosen as the baseline configuration for this test case.

Figure 8 shows a comparison of the computed pressure distribution for the wing on the splitter plate with the inviscid wind tunnel wall and the final configuration of the wing directly mounted to the viscous TDT wall. Conditions for this simulation correspond to the M = 0.825, α = 2.0° steady case. These computations were performed using the CFL3D structured grid Reynolds-Averaged Navier-Stokes (RANS) code, but similar results were also obtained using the FUN3D unstructured grid RANS solver. The change in shock location is dramatic, even though the lower surface pressures and the pressure ahead of the shock are only slightly affected by the presence of the viscous wind tunnel wall. The upper surface pressure correlation with the experimental data is still imperfect, but the shock position is much improved when the wind tunnel wall is modeled as a viscous surface.

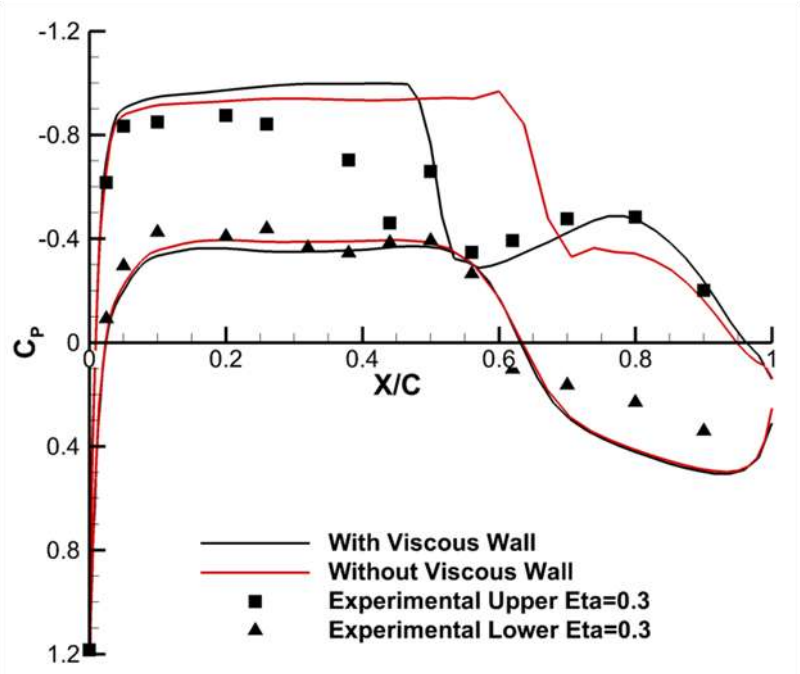

Figure 8: Computed RSW steady pressure distribution with and without viscous wind tunnel wall modeling, M = 0.825, α = 2.0°, η = 0.309.

Six analysts computed the RSW test case. The steady cases will be discussed first, beginning with the M = 0.825, a = 2.0° case. The upper and lower surface pressures computed by each analyst at η = 0.309 are compared with experimental data in Figure 9. In this figure, the computational data is shown as black solid lines and the experimental data is the white circles. All of the data provided by the analysts is shown on this plot with no regard to the individual analyst, type of method, turbulence model, or grid size. All computations shown on this plot were RANS methods using both structured and unstructured grid formulations. The majority of the analyses used the Spalart Allmaras turbulence model. The upper surface pressures are shown in the left figure, and the lower surface pressures are compared in the right figure. On the lower surface, and ahead of the shock on the upper surface, the various computational methods compute a relatively consistent set of results. However, the shock location varies widely at this span station. The results can generally be grouped into two distinct sets, those predicting a forward shock location at approximately 50 percent chord, and those with an aft shock at 65 percent chord. One set of data exhibiting the aft shock location modeled the wing from the splitter plate outboard, with an inviscid wind tunnel wall. This explains the aft shock location for some of the data shown in the figure. However, some of the aft shock cases did model the problem with the viscous wind tunnel wall. The majority of the analysts submitted a coarse, medium, and fine grid simulation for this case, and all of the grid resolutions are represented on this plot. An examination of the variation of shock locations with grid resolution showed that none of the analysts predicted a shift in the shock location that went from the aft shock set of data to the forward position as a result of improved grid refinement. The upper surface experimental pressure at

approximately 32 percent chord is assumed to be a bad pressure port. None of the computations predicted the experimental pressure character on the lower surface aft of about 70 percent chord. This is in the reflexed cove region of the supercritical airfoil section, and it is not clear what may be contributing to these differences, but the pressure magnitude is consistently over-predicted by all of the CFD methods.

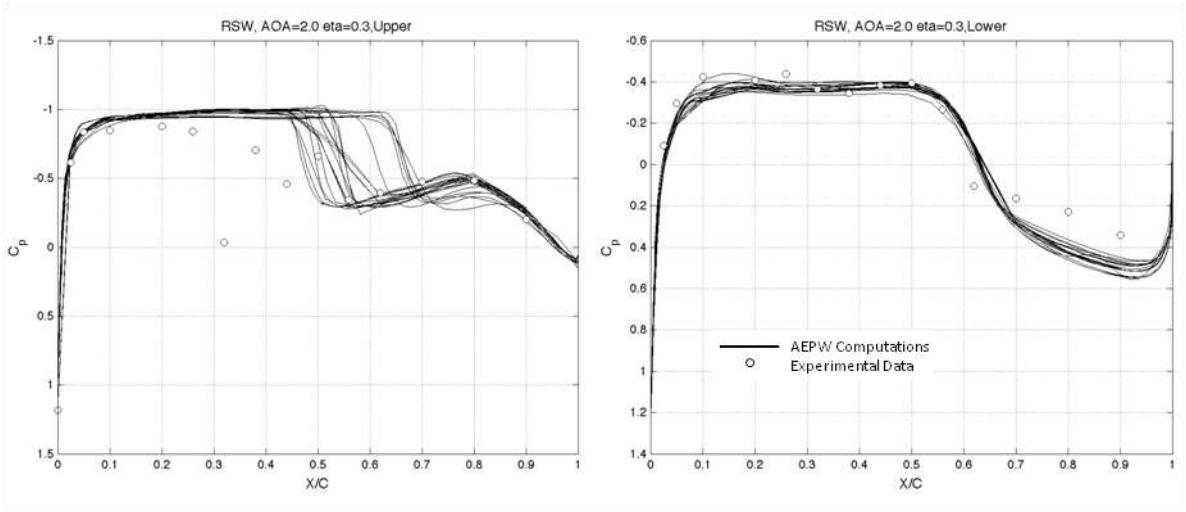

Upper Surface Lower Surface

Figure 9: Comparison of AEPW RSW steady computations with experimental pressure distributions, M = 0.825, α = 2.0°, η = 0.309.

A similar set of comparisons for the η = 0.809 span station is shown in Figure 10. At this station, which is further outboard on the wing and farther from the effects of the wind tunnel wall boundary layer, the computations predict a fairly consistent set of results and compare much more favorably with the experimental data across the entire wing upper surface. The lower surface comparisons continue to over-predict the pressure in the cove region of the airfoil. At this station, the experimental pressures at 32 percent chord on the upper surface and 45 percent chord on the lower surface are also assumed to be bad ports.

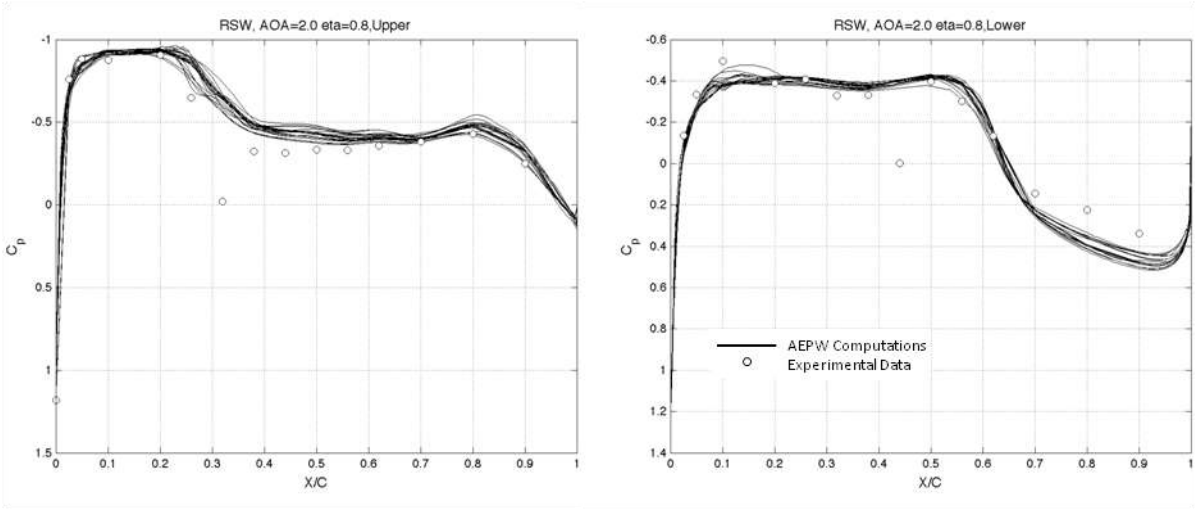

Upper Surface Lower Surface

Figure 10: Comparison of AEPW RSW steady computations with experimental pressure distributions, M = 0.825, α = 2.0°, η = 0.809.

The characteristics of the comparisons for the $\alpha = 4°$ case are similar to those presented for the $\alpha = 2°$ case and won't be presented in this paper. Again all results are available on the AePW website at https://c3.nasa.gov/dashlink/projects/47/.

The unsteady RSW results are presented next. Figure 11 shows the magnitude of the fluctuating component of the unsteady pressure scaled by the amplitude of the pitching oscillation in radians. This case represents a 10 Hz pitch oscillation of the wing, and comparisons are shown for the inboard, $\eta = 0.309$, wing station. Again, the computations predict a relatively consistent set of results on the lower surface and on the upper surface ahead of the now oscillating shock. Also note that the lower surface data on the right is plotted on an expanded scale compared to the upper surface data on the left, so the variation between the computations appears to have a higher spread than on the upper surface ahead of the shock. This is more an artifact of the plotting scale than the variation of the results. On the upper surface, the large pressure pulse represents the fluctuating shock strength and range of shock motion. There is significant variation among the computations in the location and range of the shock motion. Like the steady cases, there appears to be two predominant predicted shock locations, one in the 50 percent chord range and the other at about 65 percent chord. The methods predicting the forward shock location generally predict the same maximum value for the fluctuating pressure magnitude. It is difficult to determine the maximum pressure value for the experimental data since there is no guarantee that the limited number of pressure ports in the vicinity of the shock are located at the precise peak location. As with the steady data, these plots represent various levels of grid refinement, and the data also represents varying levels of temporal refinement ranging from 100 to 800 time steps per cycle of airfoil motion.

Figure 12 presents the same comparison at the $\eta = 0.809$ span station. At this more outboard station, the computations again show a fairly consistent character, predicting the shock location within about five percent chord of each other. The computed magnitude of the lower surface pressure is consistently larger than that of the experiment ahead of about 50 percent chord, but again all of the computations are predicting the same general character and magnitudes.

Phase plots for the fluctuating pressures for this case are also available, but for brevity are not presented here. In general, the phase data shows a similar character to the data already presented for this wing. Ahead of the shock and on the lower surface, the computational methods predict similar phase values and are in good agreement with the experimental data. But like the previous data, the upper surface shock location and the phase behavior behind the shock varies widely between the methods.

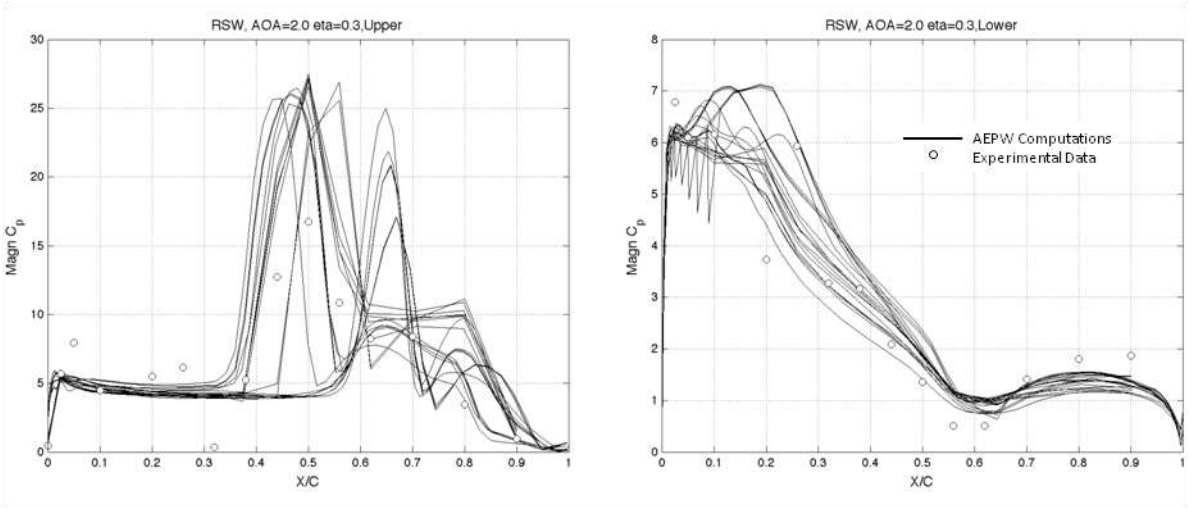

Upper Surface Lower Surface

Figure 11: Comparison of AEPW RSW unsteady computations with experimental pressure distributions, fluctuating pressure coefficient magnitude, $M = 0.825$, $\alpha = 2.0°$, $\theta = 1.0°$, $f = 10$ Hz, $\eta = 0.309$.

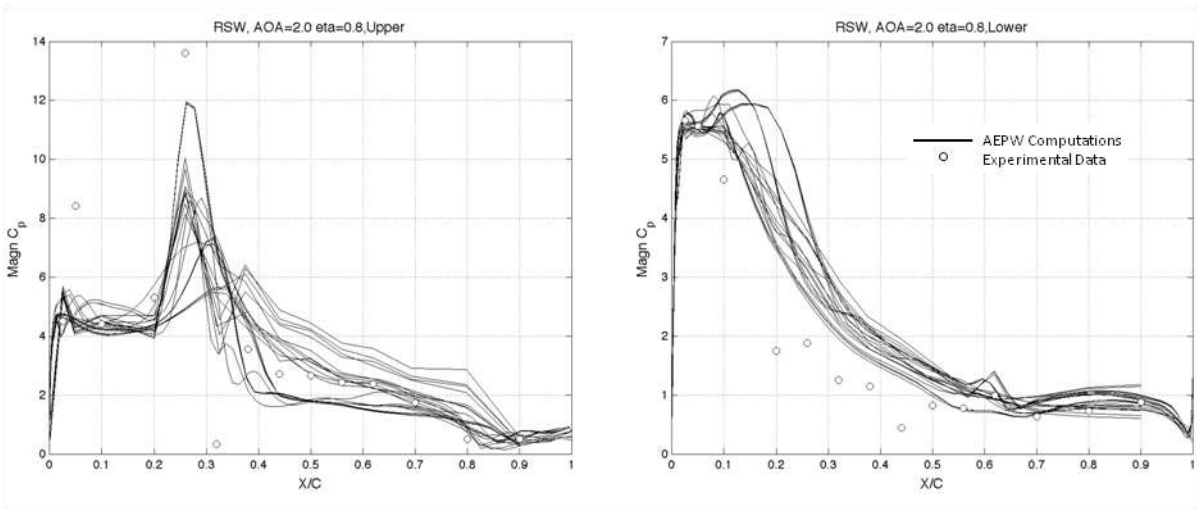

Upper Surface Lower Surface

Figure 12: Comparison of AEPW RSW unsteady computations with experimental pressure distributions, fluctuating pressure coefficient magnitude, M = 0.825, α = 2.0°, θ = 1.0°, f = 10 Hz, η = 0.809.

3.2 BSCW Data Summary

The Benchmark Supercritical Wing (BSCW) was chosen because it has a simple wing planform, there is recent comprehensive unsteady experimental data available, and these data exhibit some strong nonlinear aerodynamic phenomena. In addition, these recent data have not been widely published making it a nearly blind test case for the AePW participants. The test case was centered on a single Mach number/angle of attack combination with M = 0.85, and α = 5.0° as previously shown in Table 3. AePW participants were not supplied with the experimental data prior to performing their computations. Each analyst performed an initial set of computations at a steady angle of attack to provide an initial condition for the unsteady forced pitch oscillation simulation. The results of these steady angle of attack computations at the 60 percent wing span station are shown in Figure 13. As with the RSW case, the BSCW computations are consistent across the lower surface of the wing and on the upper surface forward of the predicted shock location. On the upper surface, the computations compare very favorably with the experimental data up to approximately 45 percent chord. In this case, complete time histories are available for the experimental data and the gradients and triangles represent the experimentally observed maximum and minimum pressures at each of the transducer locations. At approximately 45 percent chord, the experimental data suddenly shows a large increase in the difference between the maximum and minimum pressure coefficient, indicating the presence of unsteady shock motion. The large majority of the methods predict a shock location of between 50 and 60 percent chord, somewhat aft of this point. The majority of the methods also predict similar post shock behavior, though at an elevated pressure from the experiment. On the lower surface, the computations produce very consistent results up to the shock and like the RSW case, they tend to over-predict the pressures in the cove region of the supercritical airfoil. The computed differences in the lower surface shock location are not as widespread as on the upper surface.

The AePW analysts indicated that the static angle of attack simulations produced a mixture of steady and unsteady flow. Many of the coarse grid simulations converged to a steady state, while as the grid was refined to the finer grids, the static solutions became unsteady. Upper surface shock-induced boundary layer separation is believed to be the root cause for this unsteadiness in the static data. This forced many of the analysts to employ a fully unsteady CFD analysis of the static angle of attack case, as opposed to a steady state simulation. The unsteadiness in the static angle of attack data and the varied approaches of the AePW analysts to attack this problem are what likely lead to the wide variation in prediction of the shock location on the upper surface of the wing.

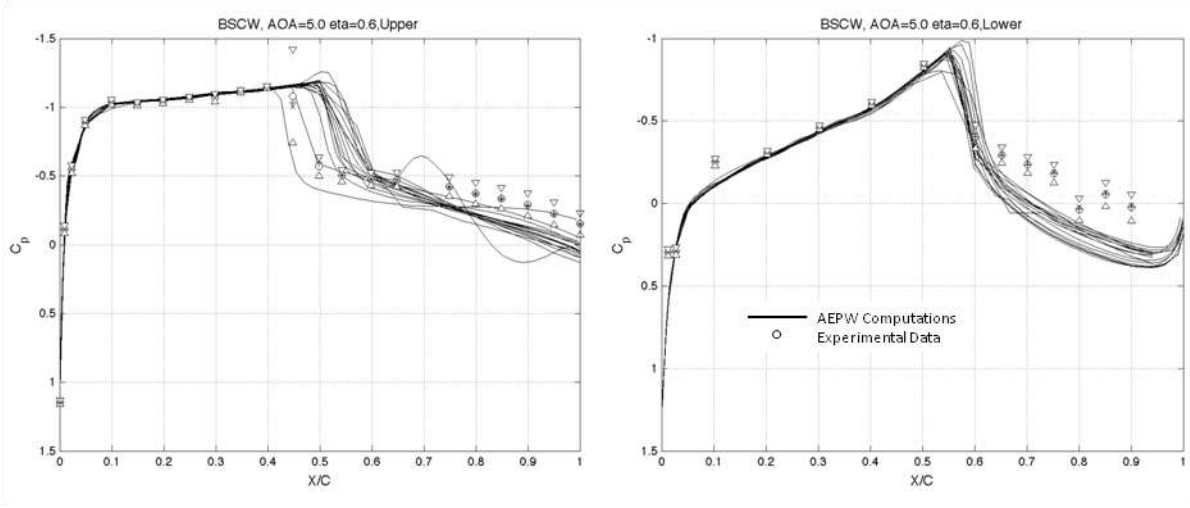

Upper Surface Lower Surface

Figure 13: Comparison of AEPW BSCW static computations with experimental pressure distributions, M = 0.85, $\alpha = 5.0°$, $\eta = 0.60$.

Two unsteady forced pitch oscillation cases were investigated, one at a relatively low frequency of 1 Hz and the second at 10 Hz for an oscillating pitch amplitude of $\theta = 1°$. The magnitudes of the computed solutions for the 1 Hz frequency case are compared to the experimental data in Figure 14. The computed data shows an upper surface shock aft of that shown in the experiment, but it is again difficult to determine the precise location of the shock in the experiment due to the placement of the pressure sensors. This is an even bigger problem on the lower surface where the experimental data does not indicate the presence of a shock at all, but all the computed results clearly show the presence of a shock at about 60 percent chord. In these two figures, the y-axis scale has changed between the upper and lower surface plots, with the upper surface scale expanded about 2.5 times larger than for the lower surface. Thus the lower surface pressure magnitude peaks are significantly smaller than the peaks on the upper surface.

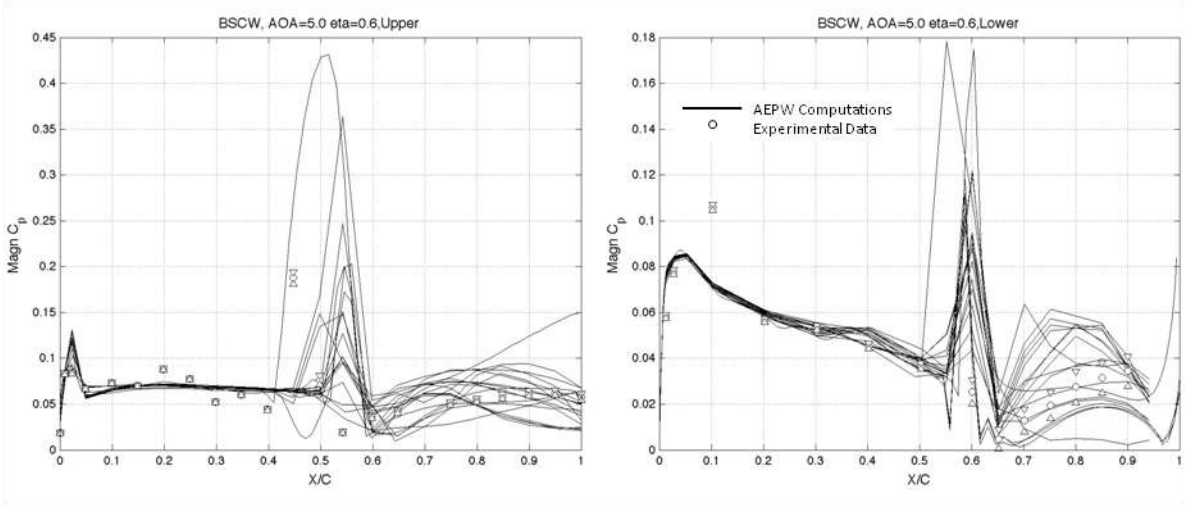

Upper Surface Lower Surface

Figure 14: Comparison of AEPW BSCW unsteady computations with experimental pressure distributions, fluctuating pressure coefficient magnitude, M = 0.85, $\alpha = 5.0°$, $\theta = 1.0°$, $f = 1$ Hz, $\eta = 0.60$.

The results for the 10 Hz Case are shown in Figure 15. Again, it appears that the majority of the AePW analysts are predicting a shock location aft of the experiment on the upper surface. On the lower surface, a shock is predicted by the computations, but the shock doesn't show up on the experimental pressures. The shock is assumed to be experimentally located between the sensors at 50 and 60 percent chord on the lower surface. The character of the predictions and their comparison to the experimental data are very similar between the two frequency cases. For both cases. The computations generally predict about the same shock location on the upper and lower surface with some fairly significant differences in the overall magnitude of the shock pressure fluctuation between the methods. The methods predict very consistent results ahead of the shocks with similar character, but large variation in fluctuating pressure level behind the shocks. As in the RSW case, phase plots for both of these cases are also available, but not presented here for brevity.

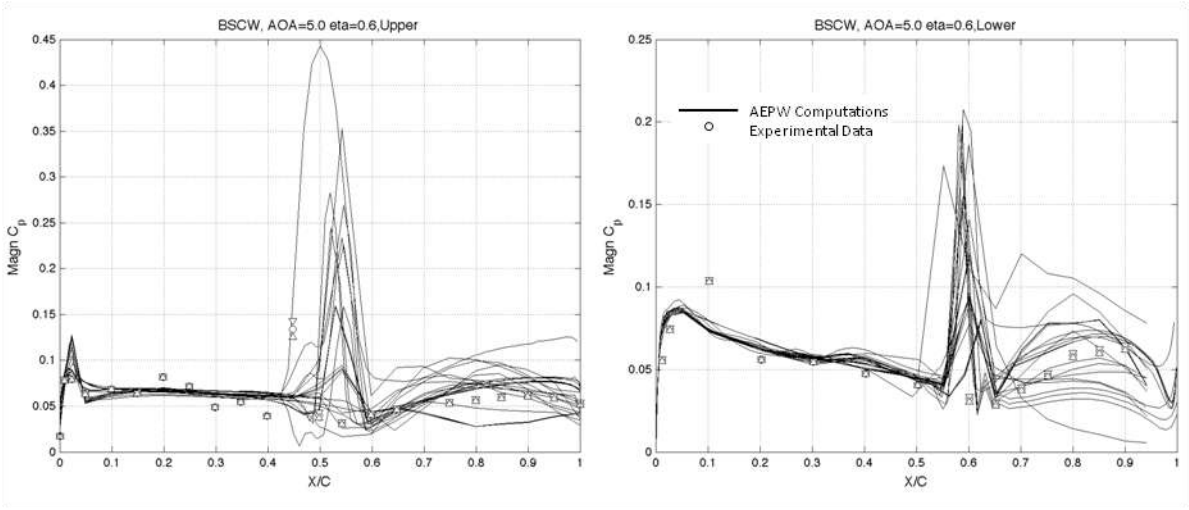

Upper Surface Lower Surface

Figure 15: Comparison of AEPW BSCW unsteady computations with experimental pressure distributions, fluctuating pressure coefficient magnitude, M = 0.85, $\alpha = 5.0°$, $\theta = 1.0°$, f = 10 Hz, $\eta = 0.60$.

3.3 HIRENASD Data Summary

The High Reynolds Number Aero-Structural Dynamics wing simulations resulted in the best comparisons among the computational methods and the experimental data. The HIRENASD Case was also analyzed by the greatest number of AePW participants. High and moderate Reynolds number cases were simulated at Mach 0.80, and the present discussion will focus on these cases, omitting the Mach 0.70 cases. Figure 16 compares the computed and experimental pressures at a steady angle of attack of 1.5 degrees, 7 million Reynolds number, and at the $\eta = 0.323$ span station. The majority of the computations predict very consistent results with excellent comparisons with the experimental data. There is some variation of the predicted upper surface shock location, but in general, the comparisons are very good. Figure 17 shows the same comparison at the $\eta = 0.804$ span station. At this station, the comparisons with the experimental data are very good with the exception of the upper surface pressures in the 20 – 35 percent chord region. Here, the computations tend to consistently predict a slightly lower pressure than that observed in the experiment.

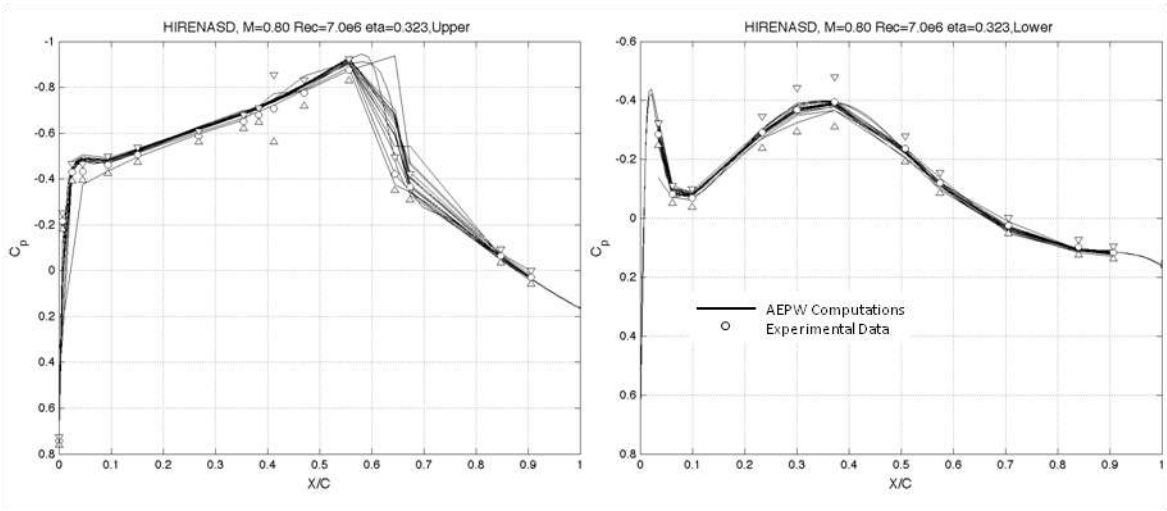

Upper Surface Lower Surface

Figure 16: Comparison of AEPW HIRENASD static computations with experimental pressure distributions, M = 0.80, α = 1.5°, η = 0.323, Re_c = 7.0 million.

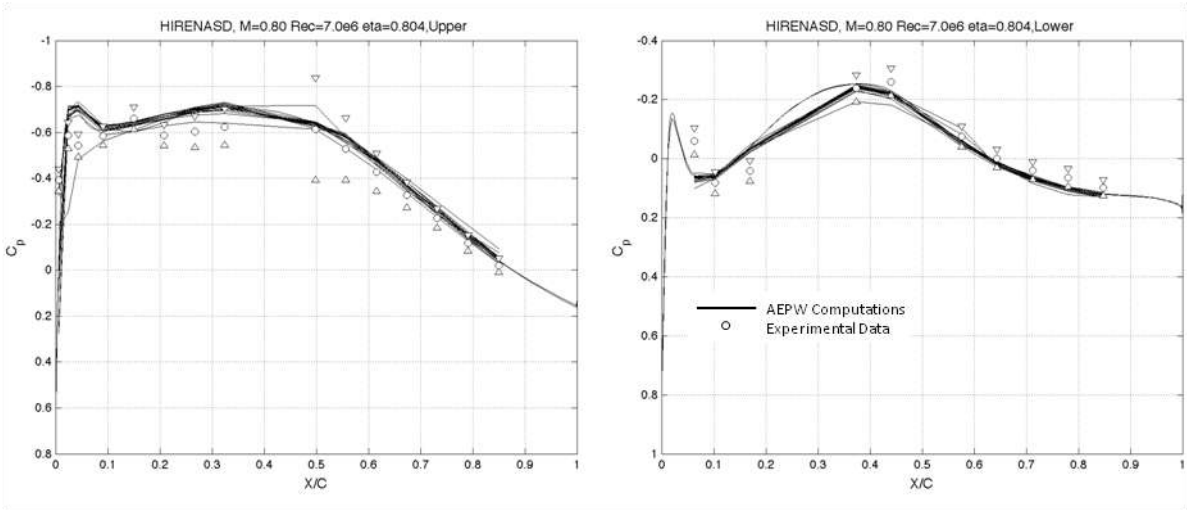

Upper Surface Lower Surface

Figure 17: Comparison of AEPW HIRENASD static computations with experimental pressure distributions, M = 0.80, α = 1.5°, η = 0.804, Re_c = 7.0 million.

Steady comparisons for the 23.5 million Reynolds number case are shown in Figure 18. The η = 0.323 span station is displayed in this figure, and the angle of attack for this case is α = -1.34°. At this higher Reynolds number, the computations continue to generally predict very consistent results, and the comparison with experimental data is very good on both the upper and lower surfaces. Results at the outboard wing station are similar in character to those presented here.

Figure 19 compares the fluctuating pressure magnitude at the η = 0.323 span station for the moderate Reynolds number unsteady case. Recall that for the HIRENASD unsteady cases, the second wing bending mode is excited at its natural frequency to generate the unsteady wing motion. The majority of the analysts simply forced the wing to oscillate in its prescribed second mode shape at the frequency and amplitude observed in the experiment. However, some of the analysts performed a coupled aeroelastic simulation where they forced the second mode shape to vibrate with a specified frequency and amplitude input, but allowed all of the structural modes to respond to the resulting unsteady aerodynamic loads. Most of the analyses predicted the same upper surface shock location, but the amplitudes vary between the analyses. The lower surface pressures are plotted on a much

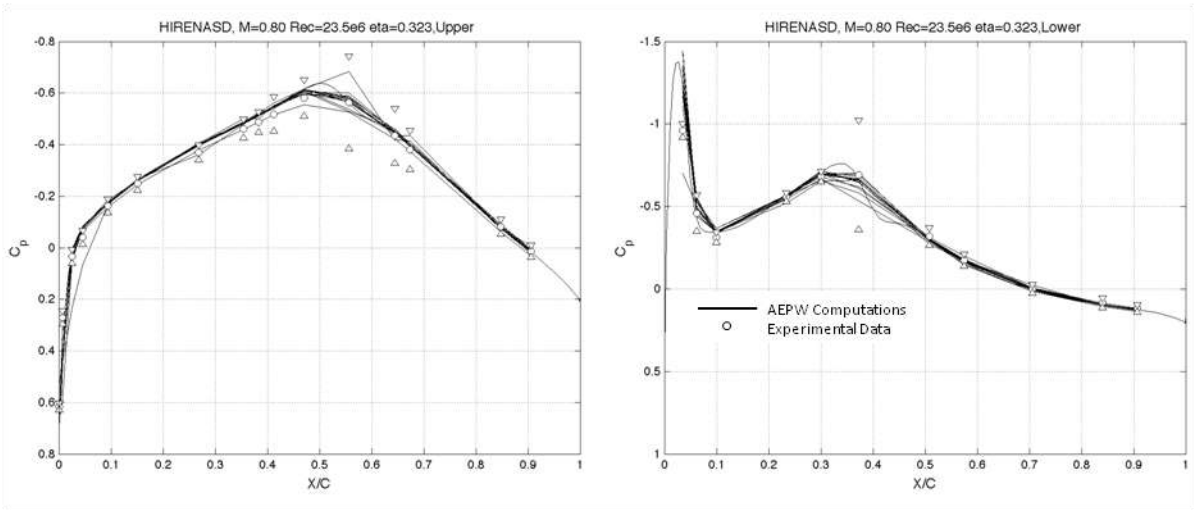

Upper Surface Lower Surface

Figure 18: Comparison of AEPW HIRENASD static computations with experimental pressure distributions, M = 0.80, α = -1.34°, η = 0.323, Re_c = 23.5 million.

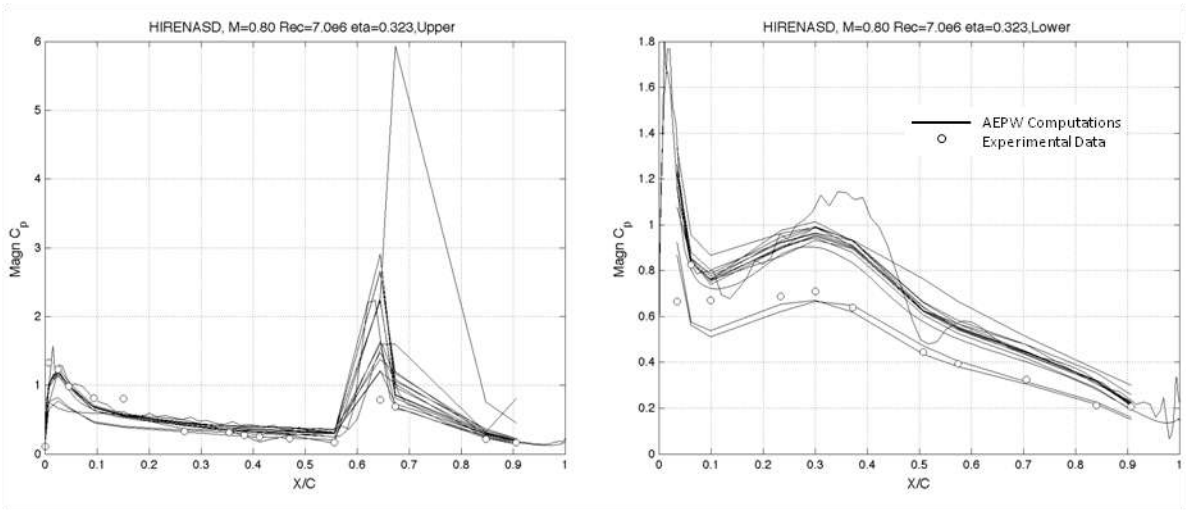

Upper Surface Lower Surface

Figure 19: Comparison of AEPW HIRENASD unsteady computations with experimental pressure distributions, fluctuating pressure coefficient magnitude, M = 0.80, α = 1.5°, Δz_t = 2.4 mm, f = 78.9 Hz, η = 0.323, Re_c = 7.0 million.

more expanded scale than the upper surface pressures, and the differences between the analyses and with the experimental data are similar to the differences on the upper surface.

Figure 20 provides the same comparison at the outboard η = 0.804 span station. Here there is a fairly wide spread in the computations on the upper surface, while the lower surface shows consistent results between the methods. The comparison with the experimental data is mixed with good correlation on the forward half of the upper surface and the computations predicting an elevated fluctuating pressure magnitude on the aft half of the upper surface. On the lower surface the comparison is good with the exception of a slightly lower magnitude prediction ahead of ten percent chord.

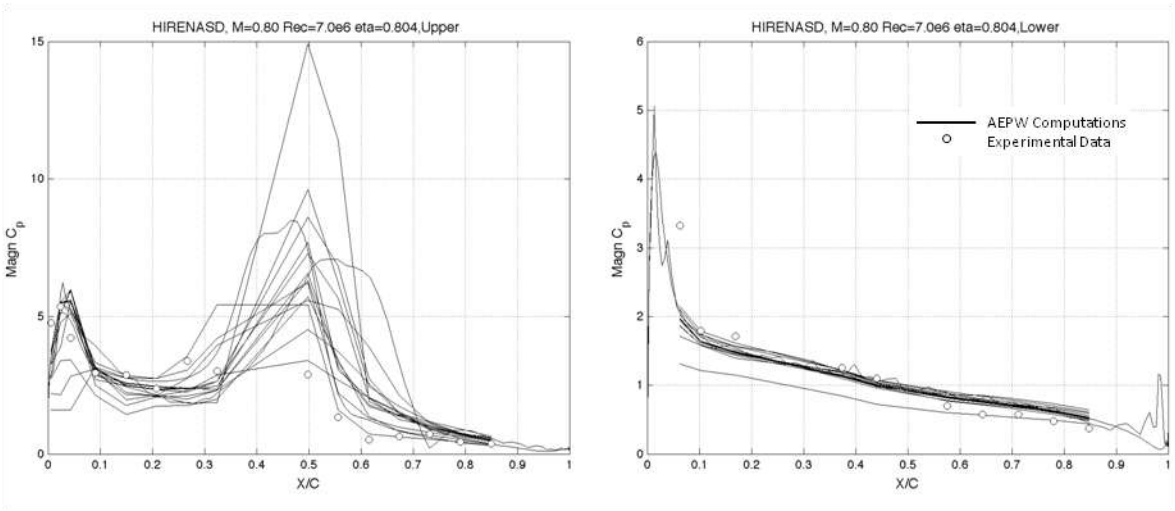

Upper Surface Lower Surface

Figure 20: Comparison of AEPW HIRENASD unsteady computations with experimental pressure distributions, fluctuating pressure coefficient magnitude, M = 0.80, α = 1.5°, Δz_t = 2.4 mm, f = 78.9 Hz, η = 0.804, Re_c = 7.0 million.

The high Reynolds number, Re_c = 23.5 Million, is shown in Figures 21 and 22. Figure 21 shows the comparison at the η=0.323 span station. Here the spread in the fluctuating pressure magnitude is noticeable on both the upper and lower surfaces, and the computations substantially under predict the magnitude ahead of 60 percent chord. The comparisons are somewhat better on the lower surface, but there is still a fairly wide spread in the magnitude of the fluctuating pressures near the wing leading edge and at the shock. Figure 22 compares the computed and experimental pressures at the η = 0.804 span station. At this station, the computational methods consistently under-predict the magnitude of the fluctuating pressure on both the upper and lower surfaces. The overall character of the pressure distributions is accurately captured by the computational methods on both surfaces with consistent pressure levels being predicted by most of the methods.

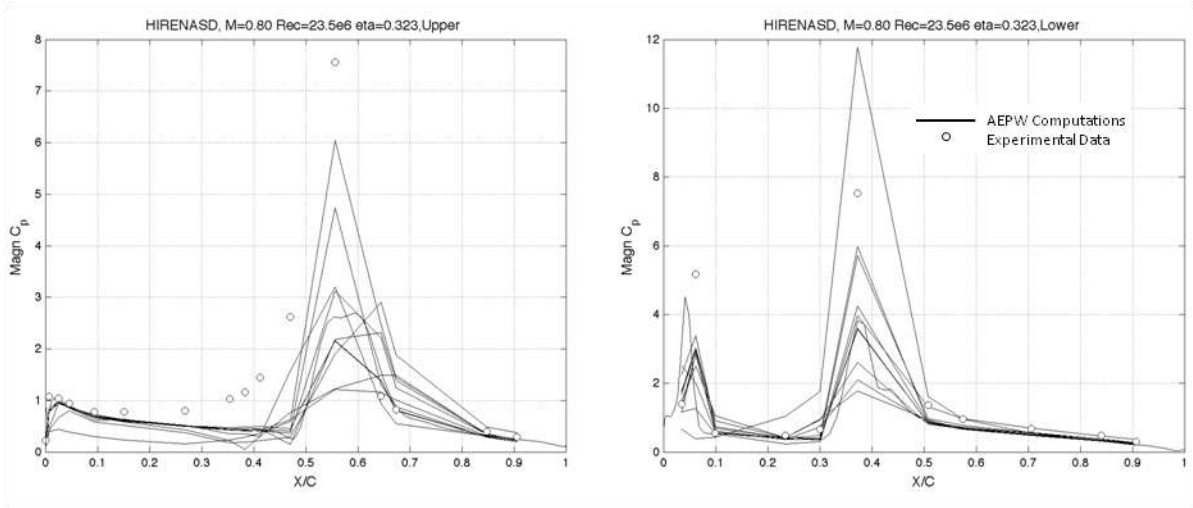

Upper Surface Lower Surface

Figure 21: Comparison of AEPW HIRENASD unsteady computations with experimental pressure distributions, fluctuating pressure coefficient magnitude, M = 0.80, α = -1.34°, Δz_t = 0.9 mm, f = 80.4 Hz, η = 0.323, Re_c = 23.5 million.

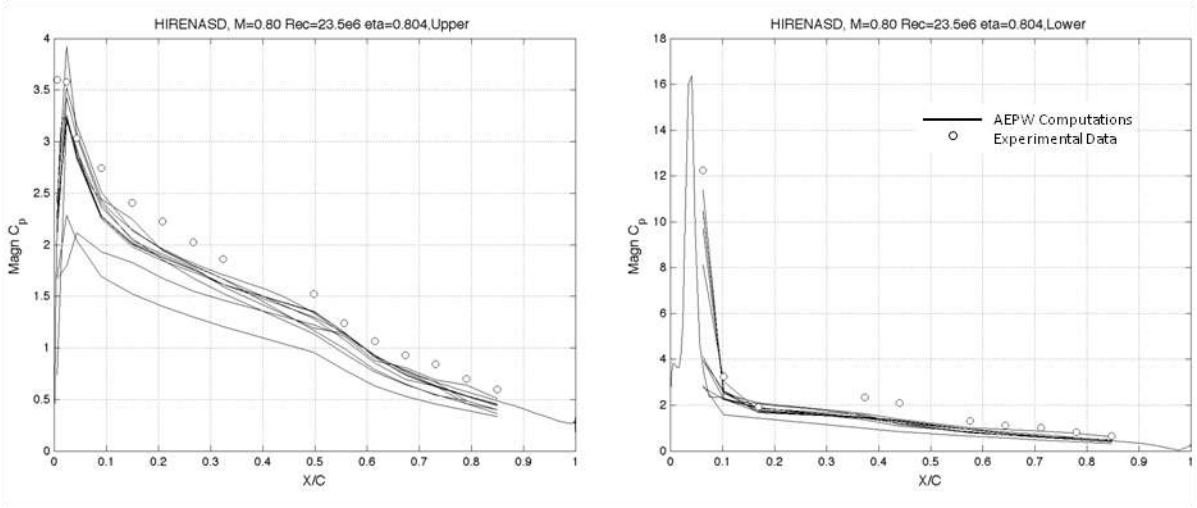

Upper Surface Lower Surface

Figure 22: Comparison of AEPW HIRENASD unsteady computations with experimental pressure distributions, fluctuating pressure coefficient magnitude, M = 0.80, α = -1.34°, Δz_t = 0.9 mm, f = 80.4 Hz, η = 0.804, Re_c = 23.5 million.

3 Summary Findings and Forward Work

There is a large volume of data still to be analyzed and understood from the first AePW, and data analysis is continuing. At the writing of this paper final data revisions from the participants had not yet been received. However, there are a number of findings that became quickly apparent as the data was initially presented and analyzed. Each of the three test cases provided some results that were surprising to both the analysts and the AePW organizers. The influence of the wind tunnel wall boundary layer was certainly unexpected when the AEPW OC chose the RSW dataset. Had this influence been recognized earlier, it may have influenced the decision to choose this test case. Equally surprising though was the wide spread in shock location predicted by the methods. As the AePW participants examined these data collectively, it was the general opinion that these results were not indicative of the proven state-of-the-art for CFD computations. Most everyone felt that the CFD should have been able to predict a more consistent shock location between the methods, even if it might have been different from the experiment. The most logical place to look for the root cause of this issue is in the modeling of the wind tunnel wall boundary layer. Therefore, to remove the wall boundary layer problem and hopefully work toward a more consistent set of results, the AePW participants are being asked to reanalyze the RSW configuration with an inviscid symmetry plane boundary condition at the splitter plate location. Given the known characteristics of the experimental setup, this will preclude any meaningful comparison with experimental data, but should provide a more consistent set of computations that are better aligned with the present state-of-the-art.

The BSCW case turned out to be as difficult as the organizers anticipated, and probably even more so. The unsteadiness in the steady angle of attack simulations was not picked up by many of the participants, and this unsteadiness appears to be a strong function of grid refinement and the choice of time step and the number of subiterations used in the time-accurate analysis. Seeing the difficulty of this case, many of the AePW participants who chose not to attempt it have now indicated that they would like to perform simulations on the BSCW. Analysts and the AePW OC are collaborating to try to define a more consistent set of grids on which to perform analyses, and further understand the role of time step and subiteration on the unsteady computation, particularly the steady angle-of-attack simulation. There is also a wealth of experimental time history data for this wing, and it exhibits highly nonlinear behavior at the chosen conditions. Each analyst submitted pressure time histories at select locations on the wing surface. Analysis and comparison of these time histories with the experimental time histories is ongoing.

Finally, the HIRENASD case was somewhat surprising since the computational methods appeared to produce the most consistent results for this case despite it being more geometrically complex. The flow conditions selected for this wing certainly weren't as challenging as those for the BSCW or the RSW, particularly when one considers the effect of the wind tunnel wall on the RSW results. Thus the comparisons with experiment were considerably improved, though there are still some noticeable differences between the theory and experiment that must be evaluated for the unsteady results.

Further analysis of these cases is expected and special paper sessions devoted to these cases are in planning for conferences in both the United States of America and in Europe. The data is open and available to anyone that is interested in performing computations on these cases and submitting results. Complete details of the Aeroelastic Prediction Workshop and how to participate can be found at https://c3.nasa.gov/dashlink/projects/47/.

References

[1] Levy, David W., et al., "Summary of Data from the First AIAA CFD Drag Prediction Workshop," AIAA Paper AIAA-2002-0841, January 2002.

[2] Rumsey, et al., "Summary of the First AIAA CFD High Lift Prediction Workshop," AIAA Paper AIAA-2011-0939, January, 2011.

[3] Ricketts, R., et al. "Geometric and Structural Properties of a Rectangular Supercritical Wing Oscillated in Pitch for Measurement of Unsteady Pressure Distributions," NASA TM-85763, November 1983.

[4] Ricketts, R., et al., "Transonic Pressure Distributions on a Rectangular Supercritical Wing Oscillating in Pitch," NASA TM-84616, March 1983.

[5] Ricketts, R., et al., "Subsonic and Transonic Unsteady and Steady-Pressure Measurements on a Rectangular Supercritical Wing Oscillated in Pitch," NASA TM-85765, August 1984.

[6] Bennett, R. M. and Walker, C. E., "Computation test Cases for a Rectangular Supercritical Wing Undergoing Pitching Oscillatios," NAS TM-1999-209130, April 1999.

[7] Dansberry, B.E.; et al., "Physical Properties of the Benchmark Models Program Supercritical Wing," NASA TM-4457, September 1993.

[8] Dansberry, B. E**.,** **"**Dynamic Characteristicso f a Benchmark Models ProgramS upercritical Wing," AIAA Paper AIAA 92-2368, April 1992.

[9] Piatak, D. J. and Cleckner, C. S., "Oscillating Turntable for the Measurement of Unsteady Aerodynamic Phenomenon," *Journal of Aircraft*, Vol. 14, No. 1, Jan. – Feb. 2003.

[10] Ballman, et al., "Experimental Analysis of High Reynolds Number Aero-Structural Dynamics in ETW," AIAA Paper AIAA-2008-0841, January 2008.

[11] Dafnis, A., et al. "Dynamic Response of the HiReNASD Elastic Wing Model under Wind-Off and Wind-On Conditions", International Forum on Aeroelasticity and Structural Dynamics, IF-073, 2007.

[12] Ballmann, J., et al. "Aero-structural wind tunnel experiments with elastic wing models at high Reynolds numbers (HIRENASD-ASDMAD)", AIAA Paper AIAA-2011-0882, January 2011.

[13] Reimer, L., et al., "Computational Aeroelastic Design and Analysis of the HiReNASD Wind Tunnel Wing Model and Tests", International Forum on Aeroelasticity and Structural Dynamics, IF-077, 2007

[14] Reimer, L., Ballmann, J., and Behr, M., "Computational Analysis of High Reynolds Number Aerostructural Dynamics (HiReNASD) Experiments," IFASD-2009-132, International Forum on Aeroelasticity and Structural Dynamics, 2009.

[15] Neumann, J., and Ritter, M., "Steady and Unsteady Aeroelastic Simulations of the HIRENASD Wind Tunnel Experiment," IFASD-2009-132, International Forum on Aeroelasticity and Structural Dynamics, 2009.

[16] Neumann, J., Nitzsche, J., and Voss, R., "Aeroelastic Analysis by Coupled Non-linear Time Domain Simulation," RTO-MP_AVT-154, 2008.

[17] Heeg, J, et al., "Plans for an Aeroelastic Prediction Workshop," IFASD-2011-110, International Forum on Aeroelasticity and Structural Dynamics, June 2011.

[18] Wieseman, C. D. and Bennett, R. M. "Wall Boundary Layer Measurements for the NASA Langley Transonic Dynamics Tunnel," NASA TM-2007-214867, April 2007.